AIAA Journal
Vol. 43, No. 6, June 2005

Experimental and Numerical Study of Hypersonic Rarefied Gas Flow over Flat Plates

Nobuyuki Tsuboi*
Japan Aerospace Exploration Agency, Kanagawa 229-8510, Japan
and
Yoichiro Matsumoto†
The University of Tokyo, Tokyo 113-8656, Japan

An experimental study of the hypersonic rarefied gas flow over a flat plate with a sharp leading edge is presented. Experiments in a low-density wind tunnel using an electron beam probe were conducted at the Shock Wave Laboratory, RWTH Aachen, Germany. Rotational temperatures for stagnation temperatures of $T_0 = 670 \sim 1000$ K and $Kn = 0.024 \sim 0.028$ based on a reference length of 0.05 m were calculated by Muntz's method and by Robben and Talbot's method. The domain of quasi-two-dimensional flow over the plate was determined from three-dimensional rotational temperature measurements. A direct simulation Monte Carlo (DSMC) method is applied to obtain a nonequilibrium state for the rarefied gas flow over the flat plate. It is shown that the numerical results agree well with the experimental results, and that nonequilibrium between the translational and rotational temperatures in the vicinity of the plate is quite large. Sensitivity analyses on the numerical results indicate that these effects exist within the uncertainty in the experimental measurements. An estimation of effective rotational collision number in an isothermal environment is carried out by the present DSMC code, and the effective rotational collision number is 3.0 at 400 K in the present gas–gas collision model.

Nomenclature

E_{rot} = rotational energy, J
g_i = degeneracy at at rotational level i
g_0 = degeneracy at ground rotational level 0
I_K = intensity at rotational revel K
K, K' = rotational revel
Kn = Knudsen number
k = Bolztmann constant
L = reference length, m
M_∞ = upstream Mach number
P_K = rotational transition probability at rotational level K
p_e = nozzle exit pressure, Pa
p_0 = stagnation pressure, Pa
p_∞ = upstream pressure, Pa
R = gas constant, J/(kg · K), or radial distance, m
Re = Reynolds number
T_e = nozzle exit temperature, K
T_eq = equilibrium temperature, K
T_0 = stagnation temperature, K
T_{rot} = rotational temperature, K
T_{tr} = translational temperature, K
T_∞ = upstream temperature, K
t_{ref} = reference time step, s
X = tangential distance from the leading edge of the plate, m
Y = normal distance from the surface of the plate, m
Z = span distance from the center of the plate, m
Z_R = rotational collision number
Z_2 = characteristic collision number based on the e-filding point
z = running collision number
y_i = rotational energy at rotational level i, J
y_0 = rotational energy at ground rotational level 0, J
λ_∞ = mean free path in upstream, m
ρ = density, kg/m^3
ρ_∞ = upstream density, kg/m^3

Introduction

RECENTLY, the development of aerospace technology has generated a strong demand on research associated with rarefied gas dynamics. The domain of rarefied gas dynamics is characterized by a flow with a large mean free path or a small representative length caused by gas low pressure and low density. The typical situation in this regime is such that the mean free path of gas molecules becomes larger than the representative length. In this rarefied gas regime, one cannot assume a continuum approach.

Space vehicles, space stations, and planetary exploration systems, which have been developed recently, fly partly in a rarefied gas environment. Their velocity is hypersonic, and their flight environment includes shock-shock interactions and shock wave-boundary layer interactions that cause high heat transfer and pressure on the body of the spacecraft, interactions that are significantly different from those on the ground. As the temperature around the body can reach a few hundred thousand Kelvin, molecules undergo chemical reactions, decomposition, dissociation, and recombination. Thus translational, rotational, vibrational, and electronic temperatures differ from one another, and the state becomes a nonequilibrium state. Carrying out a satisfying accurate experiment to simulate this experimental environment on the ground, one is faced with several problems of cost and time. Furthermore, in the numerical treatment of the problem recent advanced numerical simulation methods require much computational memory and CPU time to simulate such nonequilibrium phenomena. Furthermore, many problems remain not only in the numerical method but also in the theory of these nonequilibrium phenomena. Nevertheless it is important that the physical phenomena occurring around spacecraft in a hypersonic rarefied gas flow are studied in detail in order to understand these phenomena and to design a real size vehicle.

Received 18 May 2004; revision received 23 October 2004; accepted for publication 22 November 2004.

[*] Associate Professor, Space Transportation Engineering Department, Institute of Space and Astronautical Science, Yoshinodai 3-1-1, Sagamihara. Member AIAA.

[†] Professor, Department of Mechanical Engineering, Hongo 7-3-1, Bunkyo-ku.

The nonequilibrium phenomena occurring in such a flow have been investigated assuming that the rotational temperature is equal to the translational temperature and that vibrational and electronic temperatures are different behind a shock wave. In practice, the question of nonequilibrium between translational and rotational temperatures has not been sufficiently clarified although a full comprehension of the phenomena would be difficult without including this effect. Though many researchers tried to simulate such a nonequilibrum flow with the assumption that rotational temperature is in equilibrium with the translational temperature, numerical results fail to compare well with the experimental results.[1] This suggests that it should be necessary to take account of the rotational nonequilibrium behind the shock wave as well as the vibrational nonequilibrium.

Shock-wave and boundary-layer interaction near a sharp leading edge in a merged layer causes nonequilibrium between translational and rotational temperatures in the rarefied gas regime. A merged layer is defined as the mutual interaction between the external flowfield and the boundary-layer growth around a body of given shape. Many researchers have studied the interaction structure since the 1960s. Nagamatsu and Sheer[2] conducted experiments and showed the existence of a velocity slip. McCroskey et al.[3,4] measured density profiles over a plate as well as surface pressure and surface heat-transfer rate for a flow passing around a flat plate with a sharp leading edge. They showed that the experimental results were quite different from those predicted by the Rankin–Hugoniot relation. They also explained that this discrepancy originated in the merged layer. Vidal and Wittliff[5] and Vidal and Bartz[6,7] carried out experiments, which showed, like McCroskey, the discrepancy between the experimental data and the continuum theory. They compared the experimental results with the strong interaction theory and the weak interaction theory in detail. Vas and Allegre,[8] Chuan and Waiter,[9] and Harbour and Lewis[10] conducted similar experiments, measuring density profiles over a plate together with wall pressure and wall heat transfer. Hickman measured rotational temperatures and density distributions in a merged layer regime over a cone having a 15-deg leading edge, using an electron beam fluorescence technique,[11] but he did not discuss the question of nonequilibrium between translational and rotational temperatures.

On the other hand, the direct simulation Monte Carlo (DSMC) simulations have been done for many problems in a rarefied gas flow regime such as the studies by Bird[12] and Nanbu[13] in 1970s. Lengrand et al.,[14] Allégre et al.,[15] Chpoun et al.,[16] and Heffner et al.[17] conducted DSMC simulations and experiments for rarefied gas flow around a flat plate and explained the existence of nonequilibrium between translational and rotational temperatures from the DSMC simulations. The DSMC results agreed qualitatively with the experimental results for wall pressure and heat-transfer rate; however, the Larsen–Borgnakke model[18] used for the gas–gas collision gave only a fair estimate of the nonequilibrium phenomena. Chun[19] conducted experiments for a flat plate with a ramp and estimated a correlation between rarefaction parameter and ramp angle where a flow separation occurred. Moss et al.[20,21] and Ivanov and Gimelshein[22] used the DSMC method to compare the numerical results with their experiments. Yasuhara et al.[23] performed comparisons between the strong interaction theory, weak interaction theory, DSMC simulation, and Navier–Stokes (NS) simulation with a nonslip boundary condition and revealed the application limit for which the NS simulations hold. These studies estimated wall pressure and heat-transfer rate and compared them with experimental results; however, experimental data for translational and rotational temperatures in a nonequilibrium region over a flat plate are currently not available. Furthermore, nonequilibrium situations in the simulations were not discussed sufficiently because the molecular collision model in the DSMC simulation did not include non-Boltzmann distributions.

In this study, we use experimental and numerical methods to reveal the nonequilibrium phenomena occurring in a shock wave and boundary-layer interaction in hypersonic rarefied gas flow around a flat plate with a sharp leading edge in the case of $T_0 = 670$ K. In the experiment, the nonequilibrium rotational temperature distributions around a sharp-edged flat plate in a hypersonic rarefied gas flow exhausted from a converging-diverging nozzle were measured by an electron beam fluorescence technique. The DSMC simulations with a gas–gas collision model based on molecular-dynamic (MD) simulations were performed for similar conditions in order to reveal the nonequilibrium states in the shock-boundary-layer interaction. Finally, an estimation of effective rotational collision number was calculated for the present gas–gas collision model in order to compare with other proposed data.

Experimental Method

Experiments conducted at the Shock Wave Laboratory, RWTH Aachen, are described. Thus, freejet experiments were conducted by using the electron beam in a low-density wind tunnel.[24,25]

Experimental Setup

Figure 1 shows the schematic diagram of the wind tunnel and of the measurement facilities. The wind tunnel consists of two crossed cylinders made of steel with diameters of 1.8 and 2.4 m and lengths of 8.1 and 4 m, respectively. The net volume of the vacuum tank is 28 m^3. The wind tunnel was constructed in 1974 and has been mainly used for experiments on freejet expansions. The electron beam gun, the heating chamber, the three-dimensional transverse unit, and the optical lenses are mounted inside the wind tunnel. The spectrometer, the mass flow control facility, etc. are outside the tunnel. Water-cooling pipes coming from outside the tunnel are used to cool the electron beam gun, etc. Two rotary pumps, one roots pump, and one oil vapor booster pump are connected to the wind tunnel and allow a steady-state operation. Those pumps are

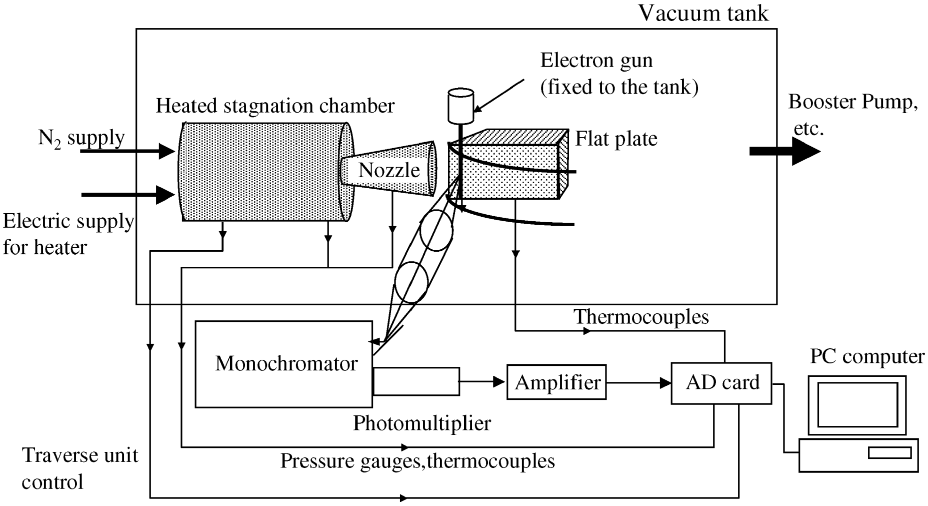

Fig. 1 Setup of measurement system.

also cooled by a closed water system connected to a heat exchanger outside the laboratory. The water-cooling system for the pumps is different from that for the electron beam gun. The final pressure with all of the pumps running is about 0.1 μbar (0.01 Pa) without gas flowing in the tunnel.

The electron beam gun is fixed to the tank top of the test section. This beam gun has a maximum acceleration voltage of 40 kV and a maximum anode current of 10 mA. This beam is sent through an orifice of about 1 mm diam into the chamber and ends in a Faraday cage. The stagnation chamber and the flat plate are connected to the transverse unit, The stagnation temperature and the stagnation pressure are measured in the stagnation chamber. Both the static pressure at the nozzle exit and the wall temperature at the flat plate are measured. The measured data are converted into electronic signals by an AD converter and stored in the PC outside the wind tunnel. The light signal of the fluorescence created by the electron beam gun passes through the lenses and is recorded by the spectrometer and the photomultiplier. Optical data are also stored in the PC. Three stepping motors connected to the transverse unit inside the tank can change the x, y, z position of the stagnation chamber. These motors are controlled by the same PC. The experimental apparatus is described in detail in Ref. 24.

Pressure Measurement

Pressures in the tank and at the nozzle exit vary from 0.01 to 300 Pa and are measured by differential pressure gauges (MSK Co.). As the pressure in the stagnation chamber and the pitot pressure vary over a wide range of values, from 10 to 2000 Pa, two absolute pressure gauges (MKS Co.) are used. To estimate the thickness of the boundary layer at the nozzle exit, the Pitot pressure was measured by a pitot-pressure probe with an inner diameter of 3.85 mm. The local Mach number and the static temperature at the nozzle exit are then calculated from the Pitot pressure data at the nozzle exit and from the stagnation pressure. The Mach number and the temperature at the nozzle exit are also calculated from the measured static pressure at the nozzle exit. In the present experiment, a static-pressure port with the diameter of 5 mm is used at a location situated 6 mm upwind from the nozzle exit.

Temperature Measurement

Rotational temperature was measured by using the electron beam fluorescence method (EBFM). This method, which was originally proposed and developed by Muntz,[26] been widely used in the past to measure the rotational temperature in a rarefied gas flow. The rotational temperature measurement by the EBFM technique has mainly been conducted in a free expansion jet for the stagnation temperature of room temperature.[26–30] When a beam of electrons is passed through nitrogen gas, a nitrogen molecule, $N_2X^1\Sigma_g^+$, with an initial electronic state E_1'', is excited to an ionized nitrogen molecule, $N_2B^2\Sigma_u^+$, with a state E' by an inelastic collision with an electron. Emission of a photon from E' brings the molecule back to an ionized nitrogen molecule, $N_2X^2\Sigma_g^+$, with a ground state E_2''. This fluorescence is called the "first negative system." To calculate the rotational temperature, the fluorescence in the R branch of the band spectrum at 391.4 nm [(0,0) transition] was measured by the monochromator. The rotational temperature is obtained from the relative rotational lines.

The rotational temperature can be calculated by three methods: the Muntz model,[26] the Robben and Talbot (RT) model,[31] and the Coe, Robben, Talbot, and Cattolica model.[32] The Muntz model uses the relation between intensity distribution in the rotational structure of the fluorescence and the initial population distribution through an appropriate model of the excitation-emission process. In the Muntz model, the excitation process uses the dipole approximation.

In an equilibrium state, the Muntz model is able to define a unique rotational temperature because all rotational levels are fitted by a straight line. However, in a nonequilibrium state a unique rotational temperature cannot be defined because nonequilibrium rotational distributions create an overpopulation of the higher rotational levels.

The RT model is based on the same concept as the Muntz model. It uses the merging of two rotational distribution functions at temperatures calculated from the lower and higher rotational levels. It defines an averaged rotational temperature T_{rot} as $T_{\mathrm{rot}} = E_{\mathrm{rot}}/\rho$, where E_{rot} is the sum of rotational energies and ρ is the density of molecules. The different between the Muntz model and the RT model is the definition of rotational temperature. The Muntz model is slope-defined rotational temperature; otherwise, the RT model defines energy-equivalent rotational temperature.

Figure 2 shows an example of rotational spectra of the (0-0) vibrational band of N_2^+ first negative system for two different slit widths. It is possible to isolate the contribution of each overlapping spectrum to the complete band by assuming each rotational spectrum to be a Gaussian distribution. The results are shown as the fitting function in Fig. 2. Using the intensities deduced from fitting the spectra, $\log(I_K/P_K)$ vs E_{rot}/k can be calculated. The results are shown in Fig. 3. The intensities are not distributed along a straight line because of the strong nonequilibrium flow over the plate. To analyze these data, we calculated two temperatures. The first one is a rotational temperature calculated by fitting the points for $1 < K < 5$ and $15 < K < 19$ with the Muntz method. The second one is calculated using the RT method in which K' is chosen as $K\max - 5$.

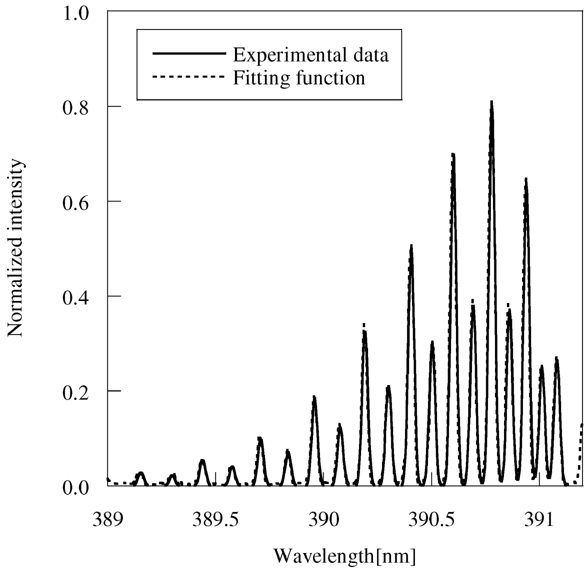

a) Run 34 with a slit width of 80 nm

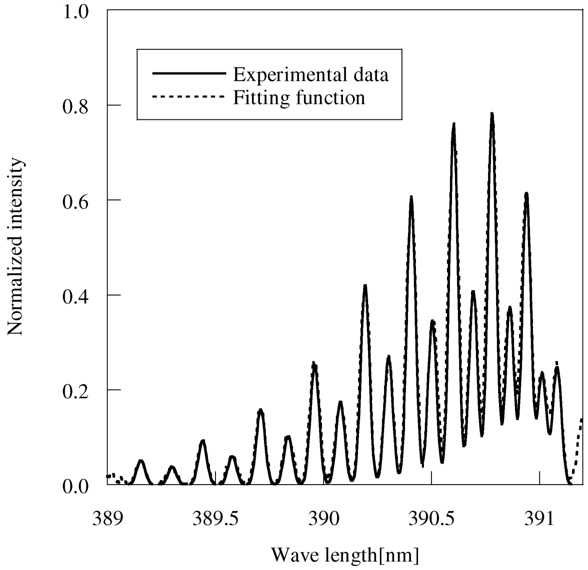

b) Run 48 with a slit width of 120 nm

Fig. 2 Rotational spectra of the (0-0) vibrational band of N_2^+ first negative system in a nitrogen flow at $X = 5$ mm and $Y = 3$ mm and the fitting function.

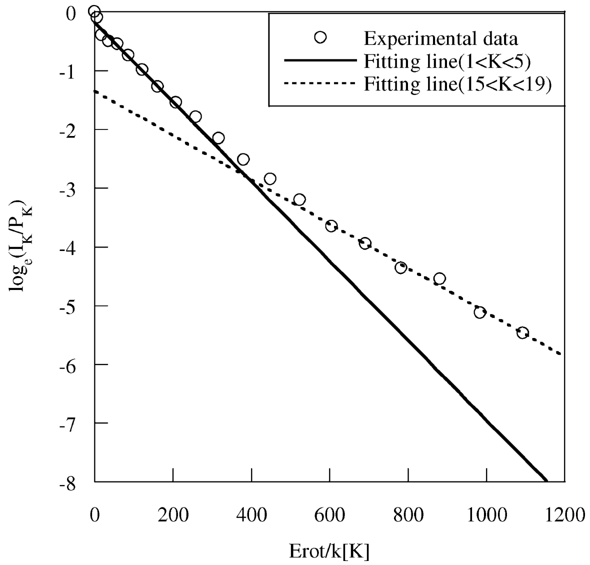

a) Run 34 with a slit width of 80 nm

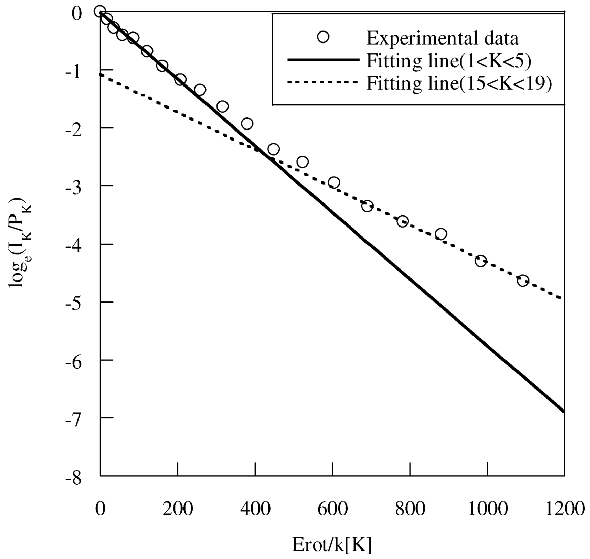

b) Run 48 with a slit width of 120 nm

Fig. 3 Plot of log(I_K/P_K) vs E_{rot}/k calculated from Fig. 2.

According to Fig. 3, K' in Eqs. (8) and (19) in Ref. 31 is set to 15. The five lowest levels ($1 < K < 5$) are fitted by the full straight line, and the five highest levels ($15 < K < 19$) are fitted by the broken straight line.

Stagnation Chamber, Nozzle, and Flat Plate

The stagnation chamber has two heat sources and three heat shields to reduce radiation. It has an effective volume of about 0.32 m^3 and is made of a stainless-steel tube with a diameter of 86 mm and a length of 300 mm. The heating element of the chamber is made of nicrome, and the empty space in the chamber is filled with ceramic balls of 5 mm diam to enhance heat transfer to the nitrogen gas. The chamber was operated to a maximum temperature of $T_0 = 1000$ K.

A convergent-divergent nozzle was designed for the present experiment (Table 1). For low-density flow, a nozzle design has to be made by using numerical analysis owing to the low Reynolds number and thick boundary layer. The numerical analysis can be conducted by two methods: The DSMC method and the NS method. The DSMC method requires a long CPU time and a finer grid system, on the order of the local mean free path, to simulate the flow caused by large variations of the local Knudsen number from the continuum regime to the rarefied regime in the nozzle. Therefore, although it is a compromise, the NS method is a more efficient tool than the DSMC method to design the nozzle. An empirical prediction can be used to estimate the boundary-layer thickness in the nozzle flow; however, the prediction provides a less accurate solution owing to the lack of experimental data.[33,34] Boyd et al.[35] carried out a DSMC simulation in a nozzle and obtained results in agreement with the experimental results; however, the design of the nozzle is not clear. Therefore, the NS method was applied to design the nozzle geometry. Wall boundary conditions used in the calculation assumed a nonslip boundary to evaluate the maximum thickness of the boundary layer.

Table 1 Nozzle geometry

Item	Value
Nozzle inlet diameter, mm	65
Nozzle throat diameter, mm	13.7
Longitudinal radius at throat, mm	6.85
Nozzle exit diameter, mm	100
Nozzle inlet half-angle, deg	45
Area ratio of exit to throat	53.18
Nozzle exit half-angle, deg	15
Nozzle length, mm	206

There are two general kinds of nozzles: the conical nozzle and the contoured nozzle. We adopted a conical nozzle design here for the following reasons: 1) it is possible to change the area ratio of throat to nozzle exit taking account of the thick boundary layer; and 2) the contoured nozzle is longer than the conical nozzle, and it is difficult to design a contoured nozzle for such a low-density flow because of the thick boundary layer in the nozzle. For the conical nozzle design, the exit half-angle and the area ratio of exit to throat have to be optimized to reduce the effect of the thick boundary layer. In the present experiments, the nozzle was designed by optimizing the exit half-angle and the area ratio of exit to throat. The nozzle was made of stainless steel. To cool the nozzle wall, a copper tube with a diameter of 8 mm for water cooling was wound around the nozzle from the throat to the nozzle exit.

The flat plate was made of copper because the plate should be cooled by water to preserve a constant wall temperature. The leading-edge angle is 30 deg, the plate thickness is 15 mm, the plate width is 100 mm, and the plate length is 130 mm. The leading edge is sharp. The distance between the nozzle exit and the leading edge of the plate is 15 mm. Thermocouples were fixed in the plate in order to measure the plate wall temperature. Two copper pipes for cooling were soldered to the lower side of the plate.

The flat plate is supported from the rear side by a straight sting. The flat plate, the stagnation chamber, and the nozzle move together, whereas the electron beam gun is fixed in the wind tunnel. The sting was mounted from the side of the stagnation chamber. The plate location, height, and angle of attack are variable by using the sting support system. As the temperature gradient normal to the plate surface can be large, the plate surface is parallel to the electron beam as shown in Fig. 1.

DSMC Method

DSMC method is a powerful technique for the numerical simulations of hypersonic flows in the rarefied regime because the continuum approach breaks down for such low-density flows. The gas–gas molecular collision model plays a significant role on the accuracy of the simulation. Larsen and Borgnakke constructed a gas–gas collision model (LB model)[18] based on the equilibrium property of the molecular energy distributions. Although such a model has been widely used, the lack of microscale phenomenon such as the T(translational)-R(rotational) energy exchange process has limited the model application.

Recently, multiscale models have been developed based on the MD simulation for a higher reproducibility of the microscale phenomena. The present gas–gas collision model [dynamic molecular collision (DMC) model], which was developed by Tokumasu and Matsumoto[36] for nitrogen molecules, is able to capture the nonequilibrium translational and rotational temperatures in a rarefied gas flow. The DMC model of diatomic molecules is based on the collision dynamics and features the cross sections and energy distributions of molecular collisions that are obtained by the MD simulations. Authors have already presented the results by using the DMC model in Ref. 37 and showed microscopic behavior such as non-Boltzmann distributions in the translational and rotational energy distributions cannot be predicted by using the LB model.

For collision-frequency calculation, the null-collision technique[38] is adopted in the DSMC simulation. The diffuse reflection model is applied to the wall boundary treatment, and the wall temperature is 290 K. These and other simulation techniques are described more detail in Ref. 37.

Results and Discussion

Experimental Conditions

Experimental conditions are shown in Table 2. The gas state at the nozzle exit is calculated from the nozzle exit static pressure.

The results of the experimental study are discussed as follows: 1) estimation of uncertainty in the measurement; 2) flowfield downstream of the nozzle exit; and 3) flowfield over the plate, a) effects of the three-dimensional flow and b) rotational temperature profiles for $T_0 = 670$ K.

First, the uncertainty in the measurement of the rotational temperature is estimated in the next section. Then the effect of the cooled nozzle wall on the boundary-layer thickness at the nozzle exit is shown. Finally, the effects of the three-dimensional flow, of the leading-edge angle, and of the stagnation temperature are evaluated from the measured rotational temperature over the flat plate downstream of the nozzle exit using the electron beam probe.

The coordinate system (X, Y, Z) in the experiment is defined as follows. X denotes the distance from the plate leading edge and is parallel to the plate surface. Y denotes the distance from the plate surface in the direction normal to the plate. Z is perpendicular to X and Y along the transverse direction of the plate. The origin is at the leading edge, on the symmetry line on the plate surface, and its radial location equals zero.

Uncertainty in the Measurement

The uncertainty in the measurement of the rotational temperature calculated from the fluorescence was estimated from about 50 measurements at three different locations around the plate. The location, experimental conditions, and results are shown in Table 3. The slit width in the experiments at $T_0 = 1000$ K is 120 nm, and it is wider than that for $T_0 = 670$ K (80 nm) because fluorescence at $T_0 = 1000$ K was weaker than at $T_0 = 670$ K.

Table 2 Experimental conditions

Condition	Run number 26	34	48
Configuration[a]	Nozzle	PlateLE30	PlateLE30
Nozzle exit Mach number	4.85	4.89	4.92
Stagnation temperature T_0, K	680	670	999
Stagnation pressure p_0, Pa	965	983	1271
Nozzle exit temperature T_e, K	119	116	171
Nozzle exit static pressure p_e, Pa	2.18	2.12	2.64
Local Knudsen number at nozzle exit based on L[b]	0.024	0.024	0.029
Local Reynolds number at nozzle exit based on L[b]	412	422	302

[a] LE = leading-edge angle (deg). [b] $L = 0.05$ (m).

The values of (max. rotational temperature—min. rotational temperature)/2 in Table 3 are defined as the uncertainty in the measurement of rotational temperatures and are listed in Table 4. The location uncertainty is estimated to 0.5 mm because of the half-diameter of the electron beam.

The uncertainty in pitot pressure is estimated to ±0.5% of the read value.

Nozzle Exit Flow Conditions

The flow at the nozzle exit was estimated in order to measure the core region in the nozzle flow. This was done for a stagnation temperature of 680 K in run 26. Figure 4a shows the comparison between the rotational temperature obtained from EBFM, the temperature estimated from the pitot pressure, and the temperature calculated from the nozzle static pressure at the nozzle exit. Rotational temperature obtained by using the Muntz model and the RT model are plotted. Temperatures from the RT model are shown with error bars, whereas minimum and maximum values obtained from the Muntz model are plotted. The flat areas in both rotational temperatures from the RT model and temperatures obtained from the pitot pressure have a width of about 30 mm near the nozzle center. The figure shows that the temperatures measured by the three different methods agree fairly well at the nozzle center. The difference between the maximum and the minimum rotational temperature distributions for the Muntz model is small near the nozzle center; however, it is large near the nozzle walls because of nonequilibrium effects.

Figure 4b shows the pitot-pressure profiles at various locations from the nozzle exit. The nozzle exit location is $X = -15$ mm. The flat area at $X = 15$ mm is quite narrow; however, the boundary layer spreads further toward the center line at $X = 35$ and 55 mm. We consider therefore that the range less affected by the boundary layer developed in the nozzle is $X < 15$ mm.

Three-Dimensional Flow Effects

In the flow over the flat plate, the deviation from an ideal flow situation originates from basically one effect. It is the interaction between the boundary layer developed in the nozzle and the sharp leading edge of the plate. Therefore, the region where this effect takes place was estimated in experimental run number 48. The experiment has a stagnation temperature of about 1000 K.

Figure 5 shows the rotational temperature profiles downstream of the nozzle exit with the plate. Rotational temperatures are calculated by the RT model. The figure shows that in the range between $X = 3$ and 15 mm the rotational temperature profiles at $Z = 20$ mm are $10 \sim 20$ K larger than those at $Z = 0, 5, 10$ mm; however, those in the region defined by $X = 30$ mm and $Y < 5$ mm are not dependent on the Z location.

From those results, the region with a planar flow over the plate is defined by $X < 15 \sim 30$ mm, $Y < 10 \sim 15$ mm, and

Table 4 Uncertainty in the measurements of the rotational temperature

Stagnation temperature T_0, K	Uncertainty, K
670	13
1000	10

Table 3 Measurement conditions, locations, and uncertainty of the rotational temperature

Location (X, Y, Z), mm	Number of measurements	Average temperature, K	Variance	(max.-min.)/2, K	Note
(−5, 0, 0)	50	154.85	8.98	6.7	$T_0 = 670$ K
(−5, 0, 0)	50	155.45	4.18	4.3	$T_0 = 1000$ K
(10, 2, 0)	50	292.48	41.17	13.4	$T_0 = 670$ K
(10, 2, 0)	50	279.90	11.62	6.5	$T_0 = 1000$ K
(1, 1, 0)	49	252.07	21.50	10.4	$T_0 = 1000$ K

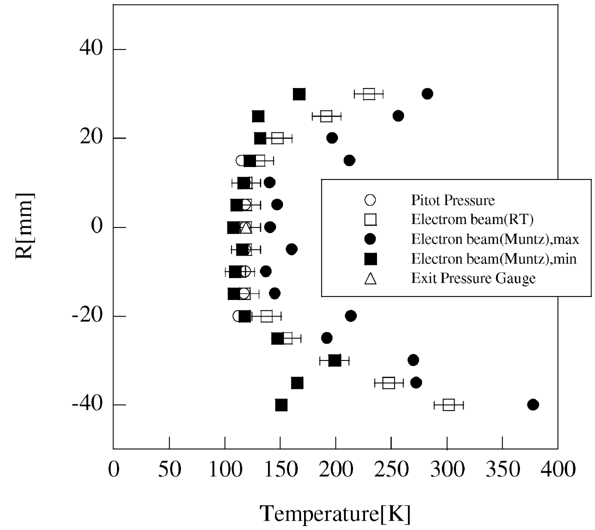

a) Temperature profiles in the nozzle exit plane

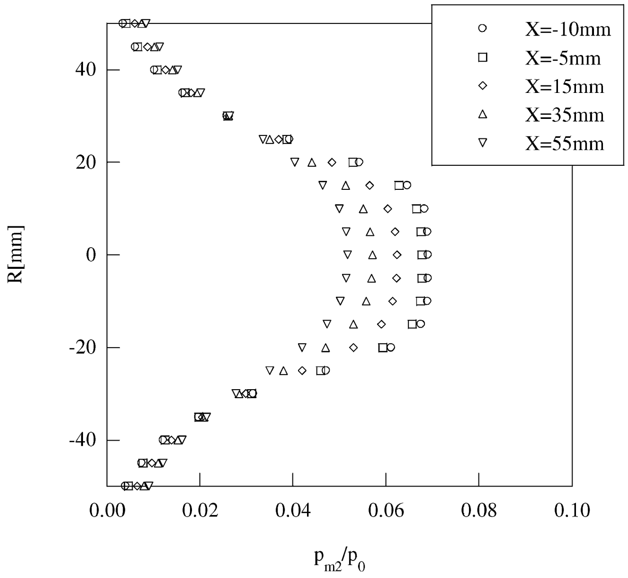

b) Pitot-pressure profiles at various locations

Fig. 4 Nozzle exit flow with wall cooling system for $p_0 = 965$ Pa and $T_0 = 680$ K.

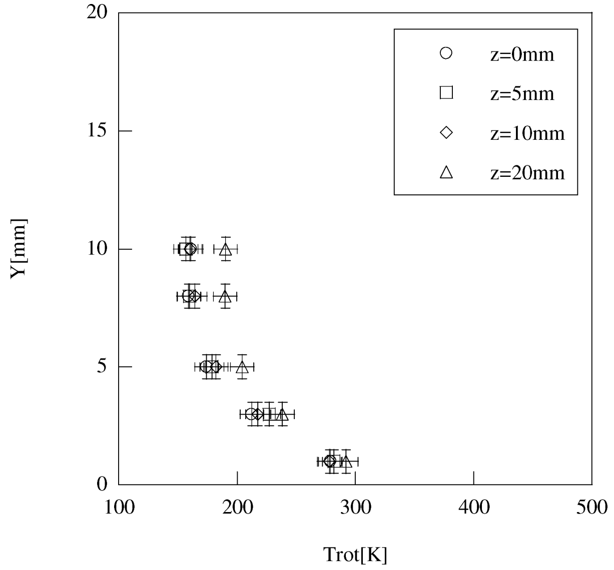

a) $X = 3$ mm

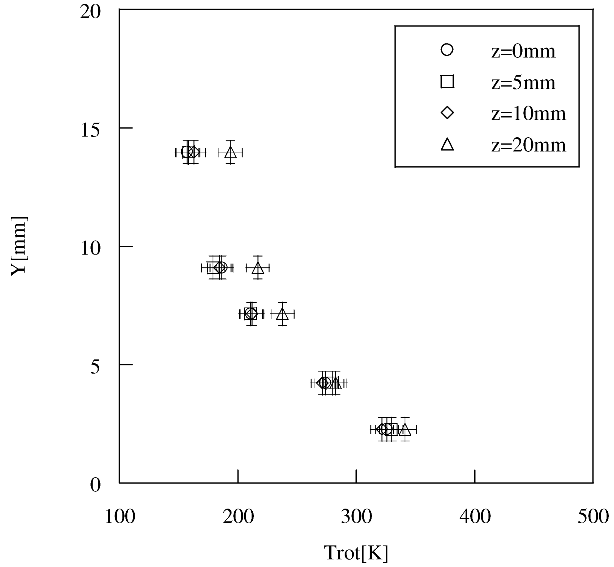

b) $X = 15$ mm

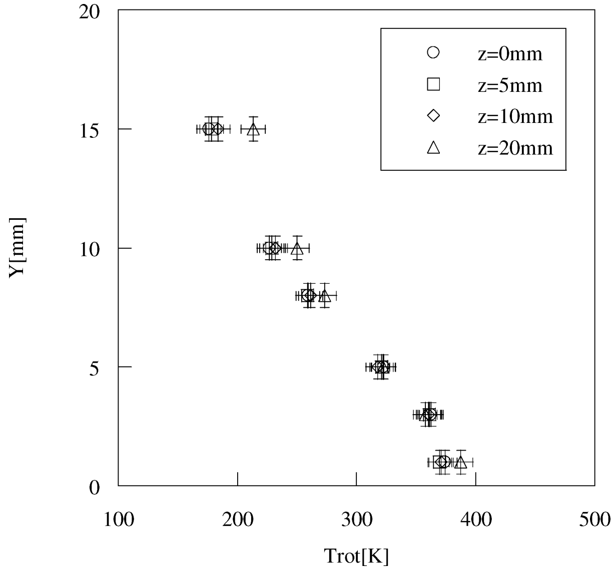

c) $X = 30$ mm

Fig. 5 Rotational temperature profiles with plate for $p_0 = 1271$ Pa and $T_0 = 999$ K.

$|Z| < 10 \sim 20$ mm. The following investigation of nonequilibrium flow is mainly discussed in this region of planar flow.

Rotational Temperature Profiles for $T_0 = 670$ K

Figure 6 shows the rotational temperature profiles at various X locations over the plate for different stagnation temperatures measured in run 34. Rotational temperatures are calculated using the RT model. The rotational temperature near the plate increases for a location far from the leading edge. Rotational temperature distributions at $Y = 1$ mm are shown in Fig. 7. The data in the figure show that the relaxation length is about 15 mm.

In front of the leading edge ($X < 0$), the rotational temperature increases and is equal to about 200 K at $X = 0$ mm because of the wedge side of the plate.

Figure 8 compares rotational temperature distributions obtained using the RT and the Muntz models. Rotational temperatures obtained by the Muntz model exhibit large fluctuations, and the difference between maximum and minimum temperatures from this model becomes large in the vicinity of the plate rather than in the freestream.

Figures 9 shows $\log(I_K/P_K)$ vs E_{rot}/k. Maxwell–Boltzmann distributions are plotted in the figures as a reference. All of the data exhibit a nonlinear variation, in agreement with the report of Robben

Table 5 DSMC simulation conditions around the flat plate

	Simulation number						
Condition	1	2	3	4	5	6	7
Grid	Normal	Fine	Normal	Normal	Normal	Normal	Normal
Number of particles	230,000	1,000,000	1,000,000	230,000	230,000	230,000	200,000
Upstream temperature T_{∞}, K	116	116	116	103	123	120	557
Upstream pressure p_{∞}, Pa	2.12	2.12	2.12	2.12	2.35	2.04	5.19
Upstream Mach number M_{∞}	4.89	4.89	4.89	4.89	4.67	4.74	1.0
Note	——	RS[a]	RS	EUC[b]	EG[c]	EG	NF[d]

[a] RS, resolution study. [b] EUC, effect of upstream condition on T_{∞}. [c] EG, effect of gradient in the flow behind the nozzle. [d] NF, nozzle flow.

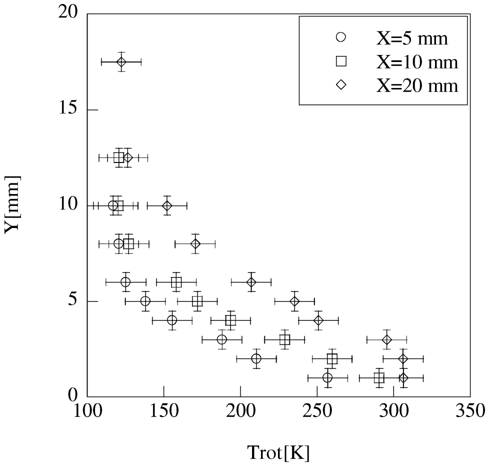

Fig. 6 Rotational temperature profiles over the plate for $T_0 = 670$ K.

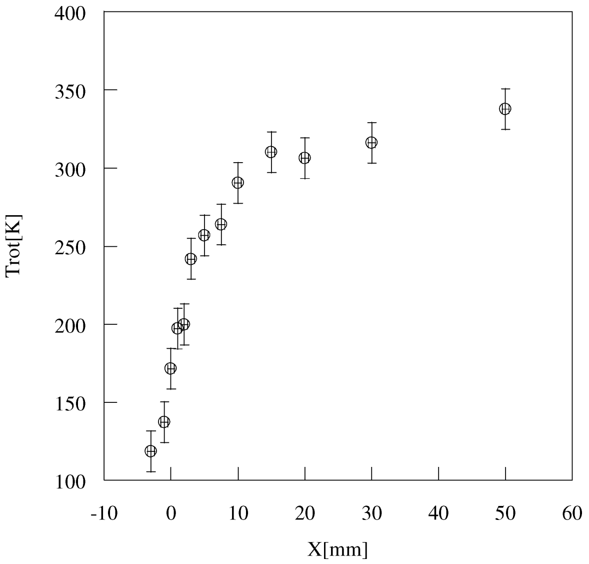

Fig. 7 Rotational temperature profiles with for $T_0 = 670$ K ($Y = 1$, $Z = 0$ mm).

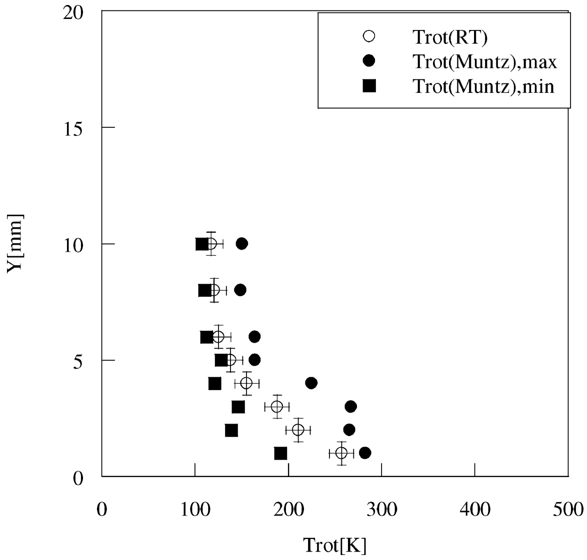

a) $X = 5$ mm

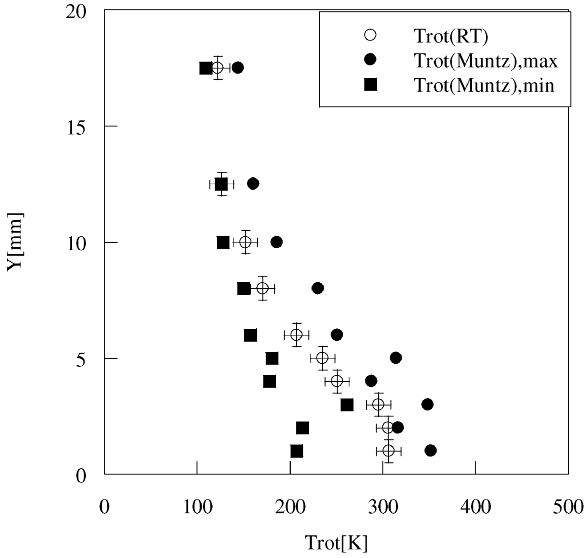

b) $X = 20$ mm

Fig. 8 Rotational temperature profiles for $T_0 = 670$ K.

and Talbot,[31] and they differ from the Maxwell–Boltzmann distributions.

Comparision Between DSMC and Experimental Results

The DSMC simulations were carried out in order to reveal the nonequilibrium effect in our experimental results. The DSMC simulation conditions are given in Table 5. Figure 10 shows the computational grid, density, and temperature contours around the plate for no. 1. A nonuniform grid system with 58 × 41 cells over the plate and with 45 × 18 cells under the plate was used for the simulations. The number of cells is approximately 3200. Time step is normalized by $t_{\mathrm{ref}} = \lambda_{\infty}/\surd(2RT_{\infty})$, and the value in the present simulation equals 0.01. The time-step effect was investigated in Ref. 37 and is concluded to be small when the value is approximately 0.01. A weak shock wave generated over the plate is clearly observed because of the thick boundary layer developed from the leading edge. Another strong shock wave also appears under the plate because of the wedge side of the plate. A nonequilibrium effect between translational and rotational temperatures appears in the vicinity of the leading edge as shown in Fig. 10e. Figure 11 shows the comparison of rotational temperatures over the plate between the DSMC and experimental results. Rotational temperatures in the DSMC simulations were calculated by the method similar to the Robben and Talbot method.

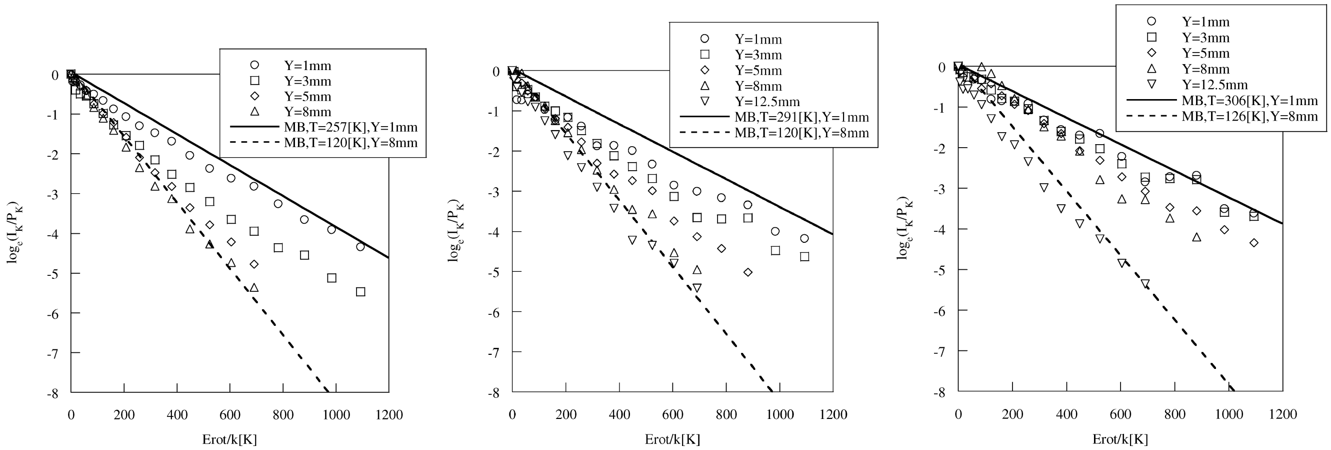

a) $X = 5$ **mm** **b)** $X = 10$ **mm** **c)** $X = 20$ **mm**

Fig. 9 Plot of log(I_K/P_K**) vs (**E_{rot}/k**),** $T_0 = 670$ **K.**

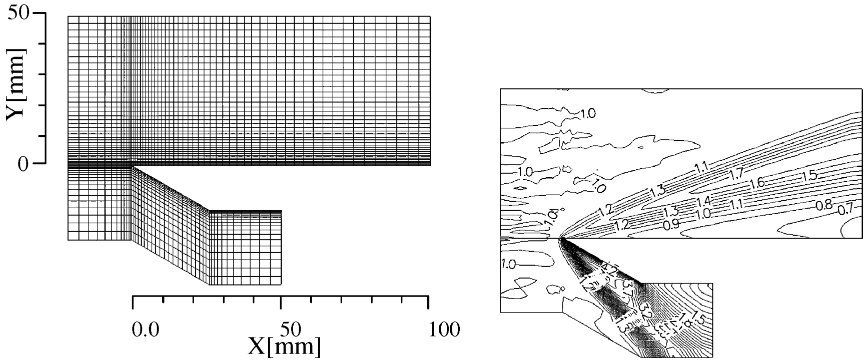

a) Computational grid system **b) Density** ρ/ρ_∞

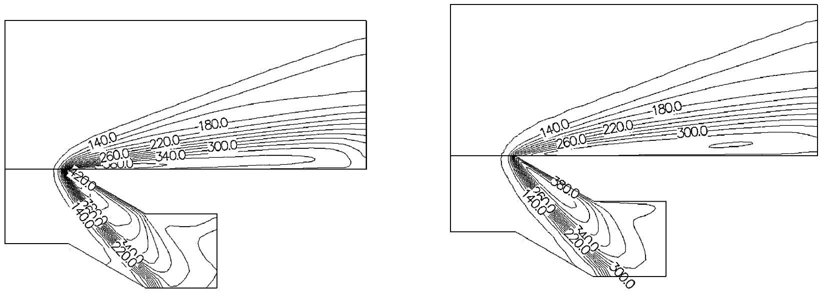

c) Translational temperature T_{tr}**, K** **d) Rotational temperature** T_{rot}**, K**

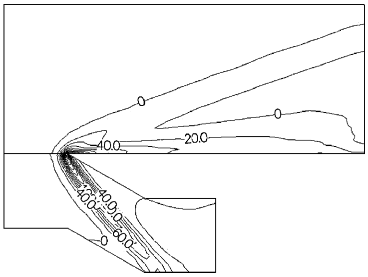

e) T_{tr}**–**T_{rot}**, K**

Fig. 10 Computational grid and DSMC results around the plate.

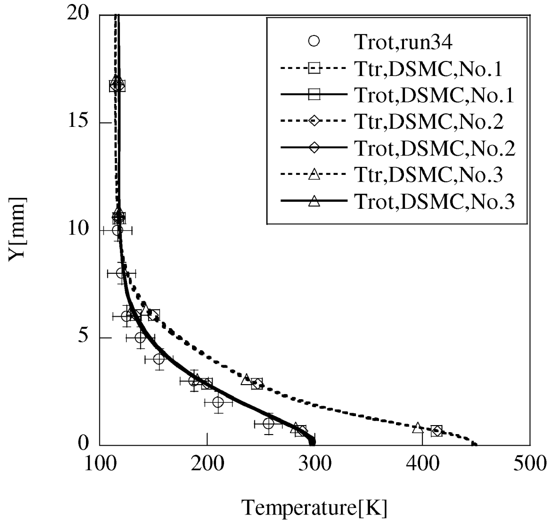

a) $X = 5$ **mm**

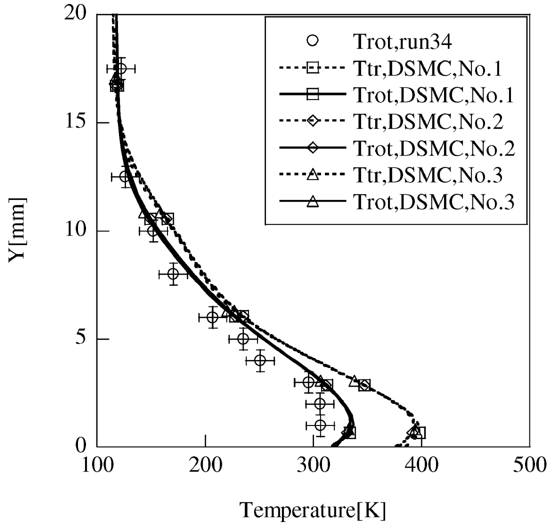

b) $X = 20$ **mm**

Fig. 11 Comparison between DSMC and experimental results. These figures also show the results of resolution study.

The DSMC results for no. 1 agree fairly well with the experimental results. Furthermore, the DSMC results indicate that the maximum difference between translational and rotational temperature is 150 K at $X = 5$ mm and that the difference reduces to about 70 K as X increases. Because of the constant wall temperature, the profiles of the translational and rotational temperatures have significantly convex shapes at $X = 20$, $Y = 1$ mm.

Sensitivity analyses in the present simulations have been done. The simulation conditions are listed in Table 5. Parameters for the sensitivity analyses are the number of computational cells and the number of particles for nos. 2 and 3. The number of computational cells is 12,800 for a fine grid. The number of particles in Table 5 is an approximate value. The results are plotted in Fig. 11, and they show that their effects do not appear in these simulations. Therefore the present normal grid and the number of particles for no. 1 are considered to be adequate when compared to the results for no. 1 and those of nos. 2 and 3.

The effect of the upstream temperature is also estimated. The upstream temperature for no. 4 in Table 5 reduces 13 K from the value for no. 1, where 13 K is uncertainty in Table 4. Other upstream values do not change from those for no. 1. Figure 12 shows the effect on the profiles of both translational and rotational temperatures when the results for no. 4 are compared with the results for no. 1. However, both temperature profiles for no. 4 decrease to approximately 20 K. The overshoot position of the translational temperature does

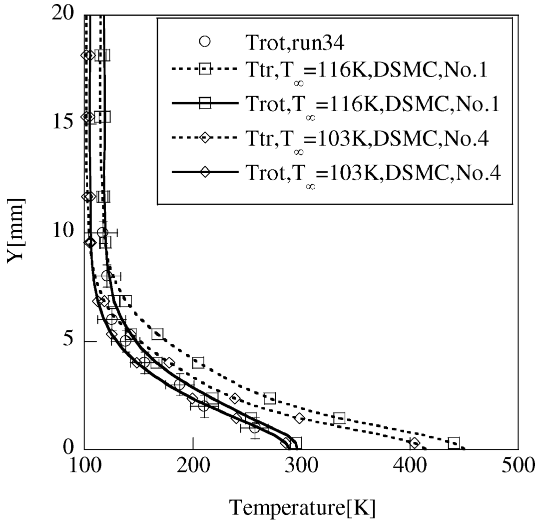

a) $X = 5$ **mm**

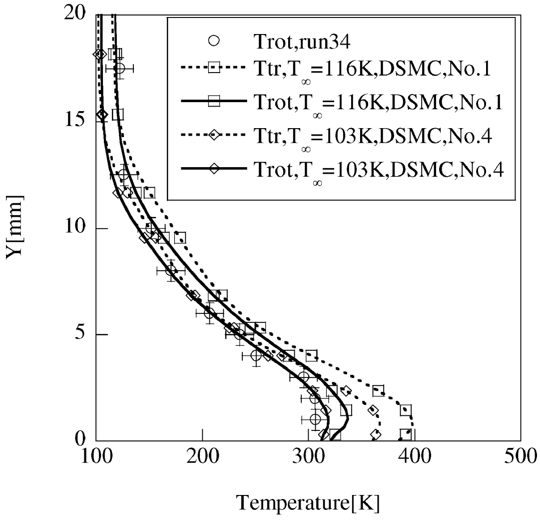

b) $X = 20$ **mm**

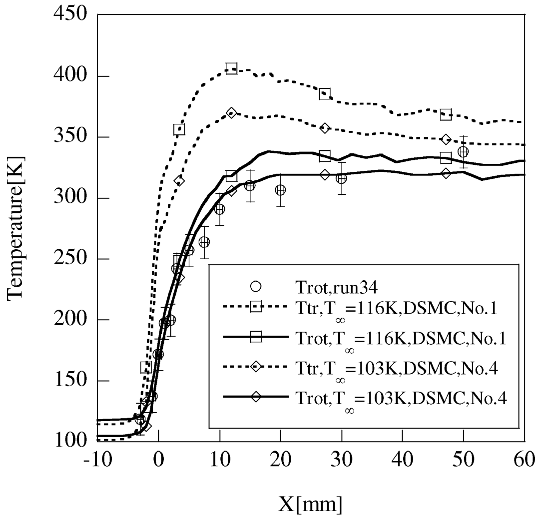

c) $Y = 1$ **mm**

Fig. 12 Effects of upstream conditions on the temperature profiles over the plate.

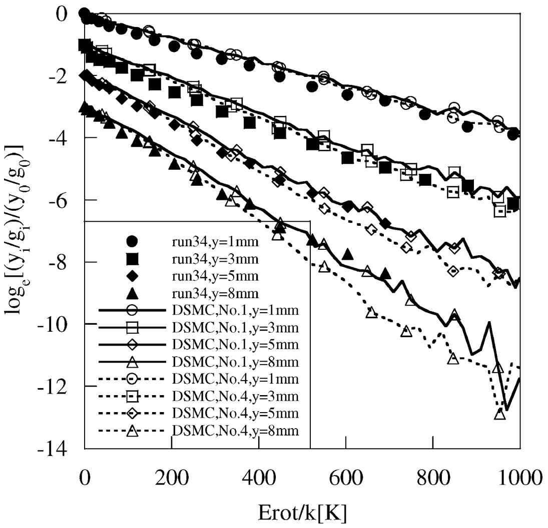

a) $X = 5$ **mm**

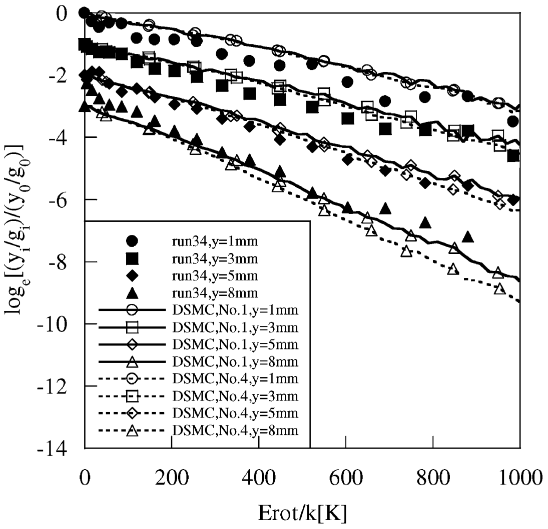

b) $X = 20$ **mm**

Fig. 13 Effects of upstream conditions on the rotational energy distributions. Vertical scale reads correctly only for $y = 1$ **mm. Add successive decrements of 1.0 to vertical scale for each lower curve.**

not change, but the decrement of translational temperature is larger than that of rotational temperature as shown in Fig. 12c. Figure 13 shows the comparison of the rotational energy distributions over the plate between the DSMC and experimental results. For the rotational energy at rotational level i in the experimental results, a degeneracy $2i + 1$ was employed; however, no degeneracy was considered in the DSMC results because the DSMC simulations did not consider the quantum effects in the rotational energy. Therefore, the number of the molecules in the range of $\Delta(E_{\mathrm{rot}})$ in the DSMC simulations was obtained, and the logarithm of the rotational energy distributions was calculated by the similar method to obtain the experimental results. In the DSMC simulations, the interval of the sample iterations was five, and sampling was conducted when the total number of particles was stable in the simulations. Figure 13 shows that the DSMC and experimental results agree well and that the non-Boltzmann distributions for both results also agree well. The effects of upstream temperature exist on the gradient especially in the higher rotational energy region.

Finally, a gradient of the flow behind the nozzle exit could exist; therefore, its effect is estimated. The simulation numbers are five and six, and these conditions are listed in Table 5. To estimate the effect, the flow inside the nozzle is calculated by the DSMC method as described earlier. The computational domain inside the nozzle begins from the throat to reduce CPU time. The wall temperature on the nozzle is 290 K, and the number of particles is approximately 200,000. Other conditions are shown in Table. 5, and its simulation number is 7. A vacuum condition is applied at the downstream boundary. These procedures are done as follows. The DSMC simulation for no. 7 is completed, then the Mach number, temperature, and pressure are obtained at $X = -10$ mm (no. 5) and $X = 0$ mm (no. 6). Because the difference between translational and rotational temperatures at these positions is approximately 5 K, both temperatures for nos. 5 and 6 assume in an equilibrium state and equal an average temperature. Therefore temperature, pressure, and Mach number at the upstream boundary are given as freestream values. The boundary layer in the nozzle is neglected here in the simulation of nos. 5 and 6.

A nonuniform rectangular grid system with 238×24 cells inside the nozzle and with 38×9 cells outside the nozzle was used for the simulations for no. 7, and is shown in Fig. 14a. The nozzle configuration is similar one as shown in Table 1. The computed Mach-number contours are shown in Fig. 14b. A significant thick boundary layer along the nozzle wall is observed and affected on a core flow at the nozzle exit. Figure 15 shows the comparison of rotational temperature between the DSMC and experimental results. In the vicinity

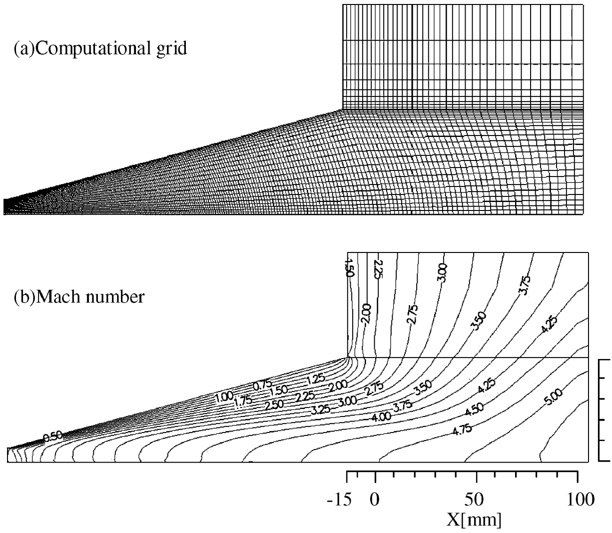

Fig. 14 Computational grid and Mach-number contours inside and behind the nozzle.

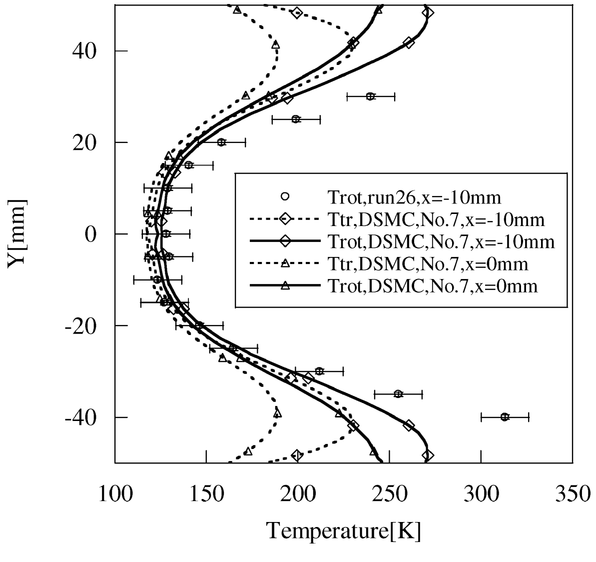

Fig. 15 Comparison between DSMC results and experimental results behind the nozzle exit.

of the nozzle center ($Y = 0$ mm), the DSMC and experimental results agree well, and the gradient of rotational temperature between these locations is small. Figure 16 shows the comparison between the DSMC and experimental results in the flow over the plate. It is clear from this figure that the effect of the gradient behind the nozzle is small.

These sensitivity analyses reveal that the freestream temperature effect exists within the uncertainty in the experimental measurement; however, the effect of the gradient of the flow behind the nozzle exit can be neglected. Finally, the nonequilibrium flow occurs over the plate, and this was quantitatively evaluated by the experimental and numerical approaches.

The choice of rotational collision number Z_R is important in simulations using the DSMC method and continuous methods because it decides a nonequilibrium state in a flow. The LB model controls the collision paramenter by using a fraction of inerastic collision ϕ. Boyd proposed ϕ and Z_R, which are dependent on temperature[39]; however, the results could not predict accurate rotational temperature distributions in a normal shock wave. On the other hand, Fujita and Abe[40] and Furudate et al.[41] directly calculated rotational collision number Z_R by using a quasi-classical-trajectory (QCT) method in a high-temperature ragime. Park[42] calculated the effective collision number Z_2 by using the numerical solutions of the master equation. To calculate Z_R, rotational relaxation time τ_R and $\mathrm{d}E_{\mathrm{rot}}/\mathrm{d}t$ have to estimate exactly[43]; however, the present DSMC method cannot calculate these values directly. Furthermore, the nonequilibrium flow over the flat plate causes not only gas–gas collision but also gas-surface interaction. Therefore it is impossible to calculate the correct Z_R by only the present DSMC results. Figure 17 shows the mean collision time in the vicinity of the plate. In a sample cell adjacent to the wall, the mean collision time between particles t_{c1} is smaller than that between particle and wall in the vicinity of the leading edge t_{c2}. The mean collision time between particles at $Y = 1$ mm, t_{c3} is approximately equal to t_{c1}. These results indicate that t_{c1} and t_{c3} are same order of t_{c2}, and nonequilibrium flow is influenced by not only molecular collision but also molecular-surface collision. Therefore an exact value of Z_R cannot be calculated from the present results. However, the effective collision number Z_2 instead of Z_R was calculated by using the present DSMC code in an isothermal environment. Z_2 was introduced in Ref. 42 and is the collision number at which $(T_{\mathrm{eq}} - T_{\mathrm{rot}})/T_{\mathrm{eq}} = 1/e = 0.3679$ of the value immediately behind the shock wave (e-folding collision number), where T_{eq} is the equilibrium temperature and is equal to T_{tr}. The effective collision number z is the ratio between the real time t and the elastic collision time. An example of the present results is shown in Fig. 18. The calculated Z_2 values are listed in Table 6. The starting postshock rotational temperature was assumed to be 1 K, which is the minimum available rotational temperature. In the present results, Z_2 is equal to 3.0 at $T_{\mathrm{eq}} = 400$ K; otherwise, Park presented $Z_2 = 4.20$ at the same equilibrium temperature.[42] The model proposed by Fujita showed $Z_R = 5.86$ at $T_{\mathrm{eq}} = 400$ K (Ref. 40). The present results are smaller than Park's and Fujita's

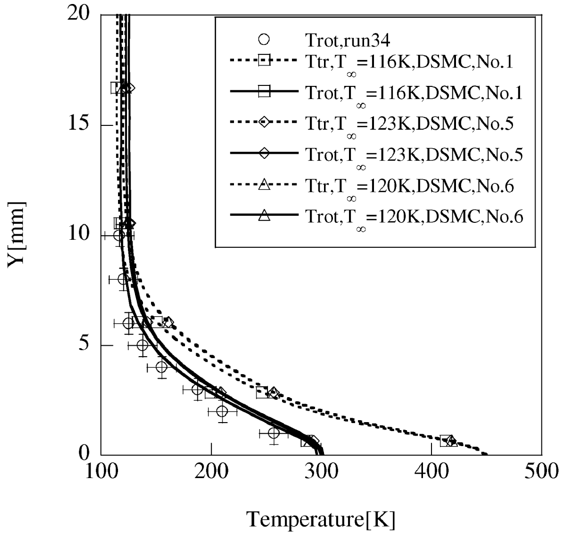

a) $X = 5$ **mm**

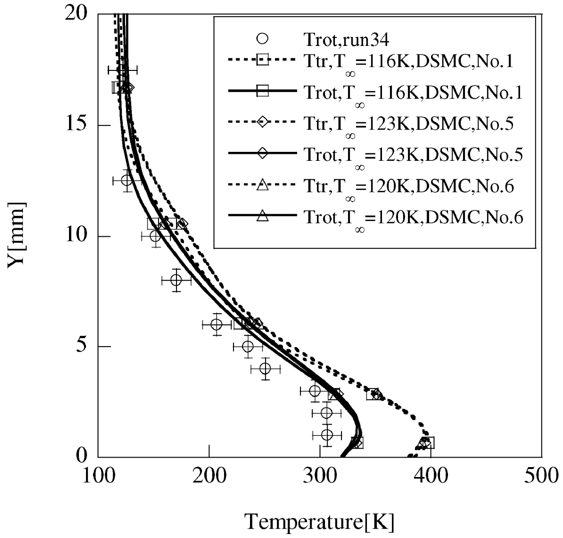

b) $X = 20$ **mm**

Fig. 16 Effect of gradient in the flow on the temperature profiles over the plate.

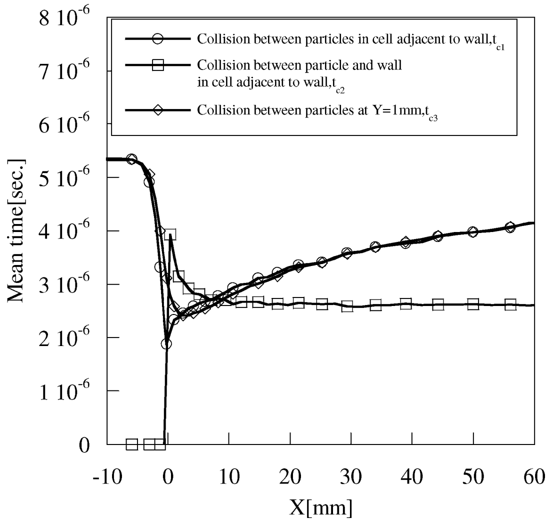

Fig. 17 Mean collision time in the vicinity of the plate.

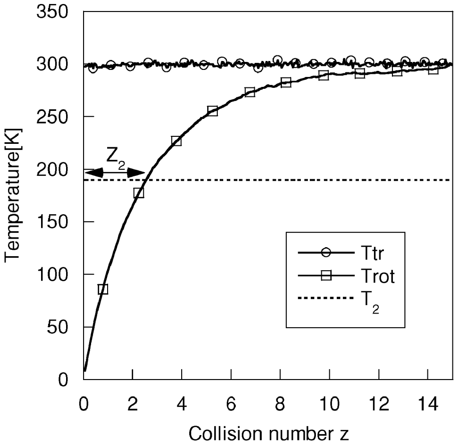

Fig. 18 Time history between translational and rotational temperatures in the isothermal environment for $T_{\mathrm{tr}} = 300$ **K.**

Table 6 Characteristic rotational collision number Z_2 calculated by DSMC simulation for fixed postshock translational bath temperature T

T_{eg}, K	Z_2
100	1.30
200	1.92
300	2.53
400	3.00
500	3.38
600	3.55

values. The value Z_R should be estimated more carefully by using other accurate simulation model in the future.

Conclusions

An experiment in a low-density wind tunnel and a direct simulation Monte Carlo (DSMC) simulation, based on the molecular simulations, were conducted to investigate shock wave and boundary-layer interaction over a flat plate in hypersonic rarefied gas flow.

An experimental system was constructed in which the effects of the boundary layer developed in the nozzle were minimized for a maximum stagnation temperature of 1000 K. For $T_0 = 680$ K, the core diameter was approximately 30 mm at the nozzle exit. The domain of the quasi-two-dimensional flow over the plate was determined by three-dimensional rotational temperature measurements. The domain of planar flow over the plate was limited by $X < 15 \sim 30$ mm, $Y < 10 \sim 15$ mm, and $|Z| < 10 \sim 20$ mm when $T_0 = 1000$ K. A comparison between the RT model and the Muntz model showed the existence of a nonequilibrium state in the flow near the plate. The similar results were shown for the rotational energy distributions.

A gas–gas collision model based on the microscale phenomena was applied to the rarefied gas flow over the flat plate by using DSMC method. It is shown that the DSMC results agree fairly well with the experimental results, and nonequilibrium between translational and rotational temperatures in the vicinity of the plate is quite large. Sensitivity analyses on the numerical results indicate that these effects exist within the uncertainty in the experimental measurements.

An estimation of effective rotational collision number in an isothermal environment is carried out by the present DSMC code, and the rotational collision number is 3.0 at 400 K in the present gas–gas collision model.

Acknowledgments

We thank the late Alfred E. Beylich from RWTH Aachen for making available his low-density wind tunnel and the diagnostic facilities, as well as providing financial support for one of the authors (Nobuyuki Tsuboi) while staying at the laboratory in Aachen. Marc Havermann, now at the French–German Research Institute of Saint-Louis, designed and tested the heatable stagnation chamber; the never-ending help and advice from Marc Havermann and Anshuman Awasthi during the experiments are greatly appreciated.

References

[1] Fujita, K., Sato, S., Ebinuma, Y., Otsu, H., and Abe, T., "Emission Spectroscopy of Nonequilibrium Radiation from Behind Shock Waves at Super-Orbital Reentry Velocity," *Proceedings of the 21st International Symposium on Rarefied Gas Dynamics*, edited by R. Brun, R. Campargue, R. Gatignol, and J. C. Lengrand, Vol. 2, Cépaduès Éditions, Toulouse, France, 1998, pp. 353–360.

[2] Nagamatsu, H. T., and Sheer, R. E., Jr., "Hypersonic Shock Wave-Boundary Layer Interaction and Leading Edge Slip," *ARS Journal*, Vol. 30, April 1960, pp. 454–462.

[3] McCroskey, W. J., Bogdonoff, S. M., and McDougall, J. C., "An Experimental Model for the Sharp Flat Plate in Rarefied Hypersonic Flow," *AIAA Journal*, Vol. 4, No. 9, 1966, pp. 1580–1587.

[4] McCroskey, W. J., Bogdonoff, S. M., and Genchi, A. P., "Leading Edge Flow Studies of Sharp Bodies in Rarefied Hypersonic Flow," *Proceedings of the 5th International Symposium on Rarefied Gas Dynamics*, Supplement 4, edited by C. L. Brundin, Academic Press, New York, 1967, pp. 1047–1066.

[5] Vidal, R. J., and Wittliff, C. E., "Hypersonic Low Density Studies of Blunt and Slender Bodies," *Proceedings of the 3rd International Symposium on Rarefied Gas Dynamics*, Supplement 2, Vol. 2, edited by J. A. Laurmann, Academic Press, New York, 1963, pp. 343–378.

[6] Vidal, R. J., and Bartz, J. A., "Experimental Study of Low-Density Effects in Hypersonic Wedge Flow," *Proceedings of the 5th International Symposium on Rarefied Gas Dynamics*, Supplement 3, edited by J. A. Laurmann, Academic Press, New York, 1966, pp. 467–486.

[7] Vidal, R. J., and Bartz, J. A., "Surface Measurements on Sharp Flat Plates and Wedges in Low-Density Hypersonic Flow," *AIAA Journal*, Vol. 7, No. 6, 1969, pp. 1099–1109.

[8] Vas, I. E., and Allegre, J., "The N-4 Hypersonic Low Density Facility and Some Preliminary Results on a Sharp Flat Plate," *Proceedings of the 5th International Symposium on Rarefied Gas Dynamics*, Supplement 4, edited by C. L. Brundin, Academic Press, New York, 1967, pp. 1015–1030.

[9] Chuan, R. L., and Waiter, S. A., "Experimental Study of Hypersonic Rarefied Flow near the Leading Edge of a Thin Flat Plate," *Proceedings of the 3rd International Symposium on Rarefied Gas Dynamics*, Supplement 2, Vol. 2, edited by J. A. Laurmann, Academic Press, New York, 1963, pp. 328–342.

[10] Harbour, P. J., and Lewis, J. H., "Preliminary Measurements of the Hypersonic Rarefied Flow Field on a Sharp Flat Plate Using an Electron Beam Probe," *Proceedings of the 5th International Symposium on Rarefied Gas Dynamics*, Supplement 4, edited by C. L. Brundin, Academic Press, New York, 1967, pp. 1031–1046.

[11] Hickman, R. S., "An Experimental Study of Hypersonic Rarefied Flow over a 10° Cone," *Proceedings of the 5th International Symposium on Rarefied Gas Dynamics*, Supplement 4, edited by C. L. Brundin, Academic Press, New York, 1967, pp. 1067–1085.

[12] Bird, G. A., *Molecular Gas Dynamics*, Clarendon, Oxford, 1976.

[13] Nanbu, K., "Direct Simulation Scheme Derived from the Boltzmann Equation. I. Monocomponent Gases," *Journal of the Physical Society of Japan*, Vol. 49, No. 5, 1980, pp. 2042–2049.

[14] Lengrand, J., Allégre, J., Chpoun, A., and Raffin, M., "Rarefied Hypersonic Flow over a Flat Plate: Numerical and Experimental Results," Vol. 160, Progress in Astronautics and Aeronautics, edited by B. D. Shizgal and D. P. Weaver, AIAA, Washington, DC, 1992, pp. 276–284.

[15] Allégre, J., Raffin, M., Chpoun, A., and Gottesdiener, L., "Rarefied Hypersonic Flow over a Flat Plate with Truncated Leading Edge," Vol. 160, Progress in Astronautics and Aeronautics, edited by B. D. Shizgal and D. P. Weaver, AIAA, Washington, DC, 1992, pp. 285–295.

[16] Chpoun, A., Lengrand, J. C., and Heffner, K. S., "Numerical and Experimental Investigation of Rarefied Compression Corner Flow," AIAA Paper 92-2900, July 1992.

[17] Heffner, K. S., Gottesdiener, L., Chpoun, A., and Lengrand, J. C., "Leading Edge Effect on Rarefied Hypersonic Flow over a Flat Plate," AIAA Paper 91-1749, June 1991.

[18] Larsen, P. S., and Borgnakke, C., "Statistical Collision Model for Monte Carlo Simulation of Polyatomic Gas Mixture," *Journal of Computational Physics*, Vol. 18, No. 4, 1975, pp. 405–420.

[19] Chun, C. H., "Experiments on Separation at a Compression Corner in Rarefied Hypersonic Flows," *Proceedings of the 17th International Symposium on Rarefied Gas Dynamics*, edited by A. E. Beylich, VCH Verlagsgesellschaft mbH, Weinheim, Germany, 1991, pp. 562–569.

[20] Moss, J. N., Price, J. M., and Chun, C. H., "Hypersonic Rarefied Flow About a Compression Corner-DSMC Simulation and Experiment," AIAA Paper 91-1313, June 1991.

[21] Moss, J. N., Rault, D. F. G., and Price, J. M., "Direct Monte Carlo Simulations of Hypersonic Viscous Interactions Including Separation," Vol. 160, Progress in Astronautics and Aeronautics, edited by B. D. Shizgal and D. P. Weaver, AIAA, Washington, DC, 1992, pp. 209–220.

[22] Ivanov, M. S., and Gimelshein, S. F., "Computaional Hypersonic Rarefied Flows," *Annual Review of Fluid Mechanics*, Vol. 30, 1998, pp. 469–505.

[23] Yasuhara, M., Nakamura, N., and Tanaka, J., "Unified Plots of Hypersonic Flow past Flat Plates in Transition Regime," Vol. 160, Progress in Astronautics and Aeronautics, edited by B. D. Shizgal and D. P. Weaver, AIAA, Washington, DC, 1992, pp. 229–233.

[24] Beylich, A. E., and Richarz, H. P., "Expansion of Gas Mixtures in Free Jet," *Proceedings of the 14th International Symposium on Rarefied Gas Dynamics*, Vol. 1, edited by H. Oguchi, Univ. of Tokyo Press, Tokyo, 1984, pp. 457–466.

[25] Awasthi, A., "Measurement of Rotational Temperature in Nonequilibrium Heated Free Jets of Nitrogen Using Electron Beam Fluorescence Technique," M.S. Thesis, Dept. of Aerospace Engineering, Indian Inst. of Technology, Chennai, India, March 1999.

[26] Muntz, E. P., "Static Temperature Measurements in a Flowing Gas," *Physics of Fluids*, Vol. 5, No. 1, 1962, pp. 80–90.

[27] Muntz, E. P., "The Electron Beam Fluorescence Technique," AGARD 132, Dec. 1968.

[28] Marrone, P. V., "Temperature and Density Measurement in Free Jets and Shock Waves," *Physics of Fluids*, Vol. 10, No. 3, 1967, pp. 521–538.

[29] Marrone, P. V., "Rotational Temperature and Density Measurements in Underexpanded Jets and Shock Waves Using an Electron Beam Fluorescence," Univ. of Toronto, UTLAS Rept. 112, Toronto, April 1966.

[30] Robben, F., and Talbot, L., "Measurement of Rotational Temperatures in a Low Density Wind Tunnel," *Physics of Fluids*, Vol. 9, No. 4, 1966, pp. 644–652.

[31] Robben, F., and Talbot, L., "Experimental Study of the Rotational Distribution Function of Nitrogen in a Shock Wave," *Physics of Fluids*, Vol. 9, No. 4, 1966, pp. 653–662.

[32] Coe, D., Robben, F., Talbot, L., and Cattolica, R., "Measurement of Nitrogen Rotational Temperatures Using the Electron Beam Fluorescence Technique," *Proceedings of the 11th International Symposium on Rarefied Gas Dynamics*, edited by R. Campargue, Commissariat a l'Energie Atomique, Paris, 1978, pp. 907–918.

[33] Touryan, K. J., and Drake, R. M., Jr., "Flow Investigation in Delaval Supersonic Nozzles at Very Low Pressures," *Proceedings of the 4th International Symposium on Rarefied Gas Dynamics*, Supplement 2, edited by J. A. Laurmann, Academic Press, New York, 1963, pp. 402–435.

[34] Koppenwallner, G., "Low Density Facilities," *Advances in Hypersonic*, Vol. 1, Birkhauser, Boston, 1992, pp. 259–323.

[35] Boyd, I. D., Penko, P. F., Meissner, D. L., and DeWitt, K. J., "Experimental and Numerical Investigations of Low-Density Nozzle and Plume Flows of Nitrogen," *AIAA Journal*, Vol. 30, No. 10, 1992, pp. 2453–2461.

[36] Tokumasu, T., and Matsumoto, Y., "Dynamic Molecular Collision (DMC) Model for Rarefied Gas Flow Simulations by the DSMC Method," *Physics of Fluids*, Vol. 11, No. 7, 1999, pp. 1907–1920.

[37] Tsuboi, N., Yamaguchi, H., and Matsumoto, Y., "Three-Dimensional Direct Simulation Monte Carlo Method of Hypersonic Rarefied Gas Flow around a Sharp Flat Plate," *Journal of Spacecraft and Rockets*, Vol. 41, No. 3, 2004, pp. 397–405.

[38] Koura, K., "Null-Collision Technique in the Direct-Simulation Monte Carlo Method," *Physics of Fluids*, Vol. 29, No. 11, 1986, pp. 3509–3511.

[39] Boyd, I. D., "Relaxation of Discrete Rotational Energy Distributions Using a Monte Carlo Method," *Physics of Fluids A*, Vol. 5, No. 9, 1993, pp. 2278–2286.

[40] Fujita, K., and Abe, T., "Coupled Rotation–Vibration–Dissociation Kinetics of Nitrogen Using QCT Models," AIAA Paper 2003-3779, June 2003.

[41] Furudate, M., Fujita, K., and Abe, T., "Coupled Rotational–Vibrational Relaxation of Molecular Hydrogen at High Temperature," AIAA Paper 2003-3780, June 2003.

[42] Park, C., "Rotational Relaxation of N_2 Behind a Strong Shock Wave," AIAA Paper 2002-3218, June 2002.

[43] Parker, J. G., "Rotational and Vibrational Relaxation in Diatomic Gases," *Physics of Fluids*, Vol. 2, No. 4, 1959, pp. 449–462.

M. Auweter-Kurtz
Associate Editor